

## Article

# Theoretical Investigation of Origin of Quantized Conduction in 2D Layered Ruddleson–Popper Perovskite Heterostructure for the RRAM Applications

Umbreen Rasheed <sup>1</sup>, Muhammad Imran <sup>2,\*</sup> , Abdul Shakoor <sup>1</sup>, Niaz Ahmad Niaz <sup>1</sup>, Fayyaz Hussain <sup>1,\*</sup>, Rana Muhammad Arif Khalil <sup>1</sup>, Mohammad Alkhedher <sup>3</sup>  and Sayed M. Eldin <sup>4</sup> 

<sup>1</sup> Materials Simulation Research Laboratory (MSRL), Institute of Physics, BahauddinZakariya University, Multan 60800, Pakistan

<sup>2</sup> Department of Physics, Government College University Faisalabad, Faisalabad 38000, Pakistan

<sup>3</sup> Mechanical and Industrial Engineering Department, Abu Dhabi University, Abu Dhabi 111188, United Arab Emirates

<sup>4</sup> Center of Research, Faculty of Engineering & Technology, Future University in Egypt, New Cairo 11835, Egypt

\* Correspondence: imraniub86@gcuf.edu.pk (M.I.); fayyazhussain248@yahoo.com (F.H.)

**Abstract:** Quantized conduction achieved in layered materials offers a wide range of applications in electronics. A comprehensive analysis of electronic properties of Sr<sub>2</sub>ZrO<sub>4</sub>/TiN- and Sr<sub>2</sub>ZrO<sub>4</sub>/TaN-layered heterostructure is carried out using plane wave-based first principles calculations. To understand the origin of quantized conduction, the role of oxygen vacancies (V<sub>o</sub>s) in 2D layered Ruddleson–Popper perovskite (Sr<sub>2</sub>ZrO<sub>4</sub>) is analyzed using density of states, isosurface, and integrated charge density plots. The origin of quantized states formed near the Fermi level is proposed in terms of charge conduction layer formed at the interface. The comprehensive insight of Sr<sub>2</sub>ZrO<sub>4</sub>/TiN and Sr<sub>2</sub>ZrO<sub>4</sub>/TaN heterostructure interface is provided by shedding light on the charge redistribution from charge density and Bader charge analysis. Meanwhile, work function is calculated for the confirmation of charge conducting behavior of the two layered heterostructures. The interface of these two layered heterostructures revealed the quantized conduction phenomena which cannot be achieved with either layer alone. Stable switching achieved with TaN electrode being an important task for robust RS and solving sneak path related problem is opening roadmap for 2D layered RRAM devices.

**Keywords:** perovskite; DOS; heterostructure; layered material



**Citation:** Rasheed, U.; Imran, M.; Shakoor, A.; Niaz, N.A.; Hussain, F.; Khalil, R.M.A.; Alkhedher, M.; Eldin, S.M. Theoretical Investigation of Origin of Quantized Conduction in 2D Layered Ruddleson–Popper Perovskite Heterostructure for the RRAM Applications. *Energies* **2022**, *15*, 9410. <https://doi.org/10.3390/en15249410>

Academic Editor: Ki-Yong Oh

Received: 19 September 2022

Accepted: 2 December 2022

Published: 12 December 2022

**Publisher's Note:** MDPI stays neutral with regard to jurisdictional claims in published maps and institutional affiliations.



**Copyright:** © 2022 by the authors. Licensee MDPI, Basel, Switzerland. This article is an open access article distributed under the terms and conditions of the Creative Commons Attribution (CC BY) license (<https://creativecommons.org/licenses/by/4.0/>).

## 1. Introduction

The Internet of things, artificial intelligence, and big data analysis demand storage systems capable of performing huge, complex, and fast calculations [1–3]. Resistive random access memory (RRAM) devices more commonly referred as memristors with simple metal/insulator/metal (MIM) heterostructures perform these tasks by memorizing the history of electric current [2,4–6]. Widespread applications of RRAM can be found in the fields of domotics, flexible electronics, smart cards, aerospace, data processing, data storage, and neuromorphic computing [7]. Despite these widespread applications of RRAM, this technology remained suppressed by its own engineering of structure and material. Performance related factors including durability, reliability, and switching speed are considered to be dependent on the capability of metal electrodes to reverse resistive switching (RS) state of RS insulating material and electronic properties in the vicinity of interface [8]. Various studies elaborated the migration of V<sub>o</sub>s/anions from RS material towards electrode in the vicinity of interface as an origin of conduction mechanism involved in switching the resistance state [9–13]. Zhong et al. [14] reported the interfacial properties and instigated the movement of anions from HfO<sub>2</sub> RS material towards TiN electrode. Rasheed et al. [15] also instigated the migration of anions form Ta<sub>2</sub>O<sub>5</sub> RS

material towards TiN electrode and formation of VoS filament at Ta<sub>2</sub>O<sub>5</sub>/TiN interface. Mikhaylov et al. [16] reported the stabilized switching as a consequence of self-organization of Ta nanocrystals and oxygen exchange at the interface of their studied heterostructure and TiN electrode. Yang et al. [17] also instigated the defect dominating RS conduction mechanism of their studied Ca-doped heterostructure and reported the movement and accumulation of O anions near the electrode. Increased (decreased) concentration of VoS exhibited by formation (rupture) of conducting filament (CFs) drives the RRAM device to attain a low resistance state (LRS) and a high resistance state (HRS). Confinement of dimensions of VoS-based CFs to the atomic units resulting in quantized conduction in RRAM devices is reported in refs. [18–20]. Consequently the concept of quantized conduction is supposed to be applicable for the practical scaling down of RRAM devices and hence improving the RRAM performance by overcoming the variability and reliability issues [19,20]. However, failure of achieving the low power aspect in transition metal oxides being RS material is reported while scaling it down caused by occurrence of leakage current problem [21–23]. Currently, the incorporation of two-dimensional (2D) materials replacing conventional metal oxide RS materials is most extensively studied owing to their wide range of applications in the emerging field of memristors caused by good endurance and retention [24,25], high ON/OFF ratio [26], low power consumption [27], and fast switching speed [28] resulting in high RS performance [3,4,21,29,30]. Until now, the use of 2D layered materials including graphene [24], SnS [28], hexagonal boron nitride [26,31,32], transition metal dichalcogenides [33,34], BiOI [35], and black phosphorus [36] is reported. Xiang et al. reported fascinating 2D interfacial effects by incorporating 2D heterostructure being a RS material in their reported memory devices [37].

Layered perovskite materials are intriguing 2D layered materials used in the emerging field of electronics. Dion–Jacobson (DJ) and Ruddleson–Popper (RP) are two identified well-known categories of layered perovskite materials. Various studied elaborated DJ and RP perovskite expressed as A''A<sub>n-1</sub>B<sub>n</sub>X<sub>3n+1</sub> and A'A<sub>n-1</sub>B<sub>n</sub>X<sub>3n+1</sub>, respectively, with A'' (di-ammonium or alkali metal cation) and A' (mono-ammonium or alkaline metal cation) present as a spacer in the intruding (separating motif) layer. While A, B, and X are organic cations, divalent metal and halide anion, respectively. It is also reported that in DJ, perovskite layers show no shift or minimum displacement, but, in RP, displacement in perovskite layer stacking is reported [38–41]. Nowadays, RP materials (A<sub>(n+1)</sub>B<sub>n</sub>O<sub>(3n+1)</sub>) having 2D layered structure are attracting attention of researchers owing to their fascinating structural and electronic properties and electrochemical migration of oxygen vacancies (VoS) [42]. To the best of author's knowledge, such Ruddleson–Popper layered material is not investigated for RS applications; it is more typically RRAM devices and is still unexplored in this field even after 22 years when its very first time prediction was reported by Beznosikov et al. [43].

In this work, RP perovskite is Sr<sub>2</sub>ZrO<sub>4</sub> being a 2D layered material is treated as RS-layered material. To instigate the application of this innovative material in RRAM devices, structural and electronic properties are explored theoretically by employing Vienna ab initio simulation package (VASP) after attaching two different electrodes (TiN and TaN). To find the origin of quantized conduction, VoS are created in Sr<sub>2</sub>ZrO<sub>4</sub>RS-layered material and dimensions of VoS-based CFs are analyzed by isosurface and integrated charge density plots. For this purpose, special cases of single (1Vo) and two (2VoS) oxygen vacancies in Sr<sub>2</sub>ZrO<sub>4</sub> are used. The detailed conductivity mechanism and stability of all considered composites is also explored here using work function calculations with the help of potential energy line ups and formation energy. It is expected that the findings of this study will provide fascinating roadmaps in state of art material related storage devices, typically RRAM applications.

## 2. Methodology

In this work, theoretical insight of quantized conduction in Sr<sub>2</sub>ZrO<sub>4</sub> being 2D RP perovskite material with TiN(TaN) electrode to understand RS in RRAM devices is elucidated.

In this regard, first of all,  $3 \times 3 \times 1$ ,  $3 \times 3 \times 3$  and  $3 \times 3 \times 3$  supercells of tetragonal  $\text{Sr}_2\text{ZrO}_4$ , cubic TiN, and cubic TaN, respectively, were modeled theoretically using the detail of structural parameters given in Table 1. The valence electronic configuration of the constituent particles used in these calculations were Ti =  $3d^2, 4s^2$ ; Ta =  $4f^{14}, 5d^3, 6s^2$ ; N =  $2s^2, 2p^3$ ; Zr =  $4s^2, 4p^6, 4d^2, 5s^2$ ; Sr =  $5s^2$ , and O =  $2s^2, 2p^4$ . After cleaving the layer of TiN (Ti = 8, N = 8 atoms), TaN (Ta = 8, N = 8 atoms), and  $\text{Sr}_2\text{ZrO}_4$  (Sr = 12, Zr = 6 and O = 24 atoms) from these simulated supercell, two hetero-layered structures  $\text{Sr}_2\text{ZrO}_4/\text{TiN}$  and  $\text{Sr}_2\text{ZrO}_4/\text{TaN}$  were optimized (Figure 1) to instigate the conduction mechanism. All of these calculations were carried out using density functional theory (DFT) [44] by employing VASP [36]. Geometry optimization and all first principle calculations of two considered structures were carried out using generalized gradient approximation (GGA). For making calculations more accurate, Hubbard U parameters were used along with GGA to include the coulombic effect along with exchange and non-local exchange correlation functional. All calculations were performed using Perdew–Burke–Ernzerhof (PBE) and projected augmented wave (PAW) potential [45–48]. The opted value of U parameter for Ti, Ta, and Zr were 8 eV [48], 2.27 eV [49], and 2.66 [50], respectively. Convergence tests for total energy of the system with respect to wave function of electrons were conducted using a plane wave basis having cutoff energy of 510 eV. To relax the system until Hellmann–Feynman force became lower than  $0.02 \text{ eV}/\text{\AA}$  was conducted using conjugate gradient method (equilibrium structural parameters given in Table 1). Possible energy criteria of  $1 \times 10^{-5} \text{ eV}$  [51] was set and most well-known Monkhorst pack sampling technique (MPST) with  $5 \times 5 \times 7$  MP grid was employed here [52,53]. As this study aims to instigate the  $\text{V}_\text{os}$ -based interfacial RS, so  $\text{V}_\text{os}$  at interface of RS layer and electrode layer,  $\text{O}^{2-}$  atoms were removed from site where Zr–O and N–O bond length (Table 2) was lesser. Electronic properties were instigated using isosurface charge density, integrated charge density (ICD), density of states (DOS), and partial density of states (PDOS) plots. To determine the quantitative analysis of charge redistribution, a Bader charge analysis was also conducted. The work function of the considered composites was also calculated to elaborate the interfacial effects. Formation energy calculations confirmed the stability of studied composites.

**Table 1.** Equilibrium structural parameters of  $\text{Sr}_2\text{ZrO}_4$ , TiN and TaN.

Computed Parameter		$\text{Sr}_2\text{ZrO}_4$	TiN	TaN
Space group		I4/mmm	F43M	Pm3m
Point group		4/mmm	43m	m3m
Crystal system		Tetragonal	Cubic	Cubic
Oxidation state of the constitution atoms		$\text{Sr}^{2+}, \text{Zr}^{4+}, \text{O}^{2-}$	$\text{Ti}^{3+}, \text{N}^{3-}$	$\text{Ta}^{1+}, \text{N}^{1-}$
Bandgap (eV)		3.105 eV	0.00	0.00
Formation energy (eV/atom)		−3.369 eV	−1.538	−1.237
Magnetic ordering		Nonmagnetic	Nonmagnetic	Nonmagnetic
Lattice Parameters (Å)	a	3.814	4.50	2.654
	b	3.814	4.50	2.654
	c	7.528	4.50 Å	2.654
Bond angle (°)	$\alpha$	144.964	90.000	90.000
	$\beta$	144.964	90.000	90.000
	$\gamma$	49.270°	90.000	90.000

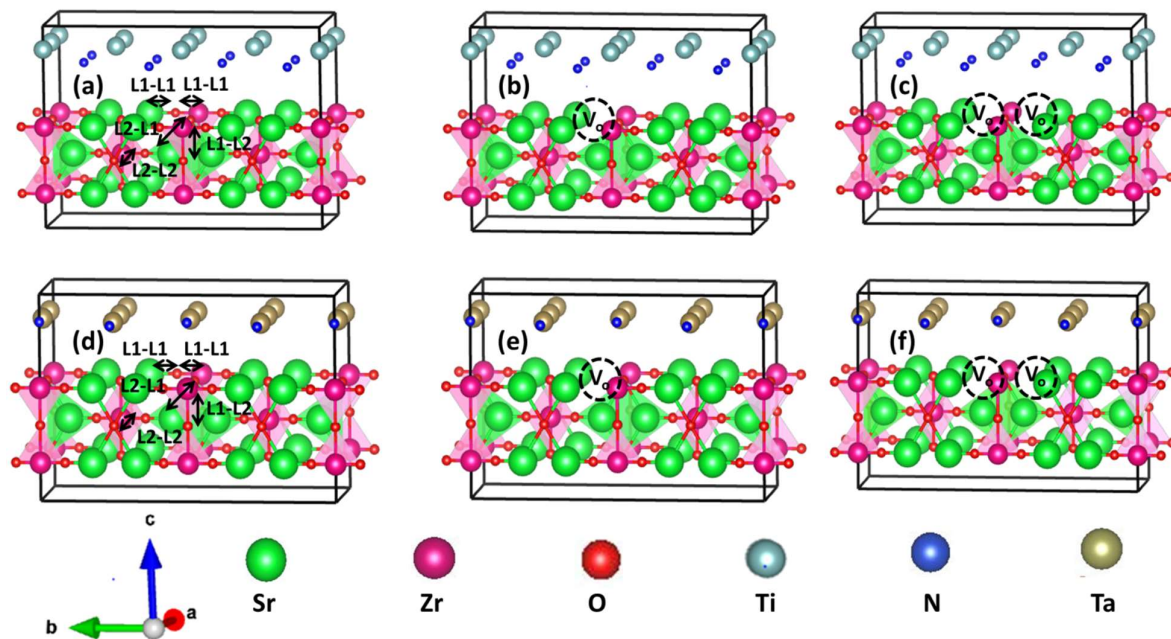


**Figure 1.** Three dimensional view of considered layer Ruddleson–Popper perovskite attached with electrode composite (a) pristine  $\text{Sr}_2\text{ZrO}_4/\text{TiN}$ , (b)  $\text{Sr}_2\text{ZrO}_4 + 1\text{V}_0/\text{TiN}$ , (c)  $\text{Sr}_2\text{ZrO}_4 + 2\text{V}_0/\text{TiN}$ , (d)  $\text{Sr}_2\text{ZrO}_4/\text{TaN}$ , (e)  $\text{Sr}_2\text{ZrO}_4 + 1\text{V}_0/\text{TaN}$  and (f)  $\text{Sr}_2\text{ZrO}_4 + 2\text{V}_0/\text{TaN}$ , respectively. Here c axis is used to stack the layers of the studied composites. Pink and green highlighted regions are indicative of octahedral and tetrahedral bonding of Zr-O and Sr-O.

**Table 2.** Bond length of the  $\text{Sr}_2\text{ZrO}_4/\text{TiN}$  and  $\text{Sr}_2\text{ZrO}_4/\text{TaN}$ .

Composite Name	Species Involved in Bond Length Calculations with Site Layer Detail		Bond Length (Å)			
			Unrelaxed Structure	Relaxed Structure		
				Pristine	Pristine + $1\text{V}_0$	Pristine + $2\text{V}_0$
$\text{Sr}_2\text{ZrO}_4/\text{TiN}$	Sr-O	(L1-L1)	1.626	1.634	1.750	1.925
		(L2-L1)	2.452	2.321	2.322	2.328
	Zr-O	(L1-L1)	1.448	1.652	1.998	1.695
		(L1-L2)	2.0875	2.085	2.073	1.908
		(L2-L2)	3.345	3.255	3.345	3.344
		Ti-N	2.603	1.628	2.572	2.518
		Ti-O	5.062	4.362	5.052	5.805
	N-O	3.863	4.047	3.870	3.906	
$\text{Sr}_2\text{ZrO}_4/\text{TaN}$	Sr-O	(L1-L1)	1.6099	1.666	1.690	1.663
		(L2-L1)	2.445	2.307	2.335	2.312
	Zr-O	(L1-L1)	1.434	1.625	1.989	1.672
		(L1-L2)	2.0875	1.995	2.106	2.040
		(L2-L2)	3.255	3.345	3.255	3.255
		Ta-N	1.627	2.52	1.628	1.626
		Ta-O	4.288	4.974	4.331	4.370
	N-O	3.968	3.901	4.017	4.055	

### 3. Results and Discussion

#### 3.1. Structural Properties

In this study, the structural properties of  $\text{Sr}_2\text{ZrO}_4$ , TiN, and TaN were instigated and the equilibrium structural parameters are tabulated in Table 1. Noting the structural parameters, two different systems modeled theoretically employed the VASP code for device to device variation of memory parameters as shown in Figure 1.  $\text{Sr}_2\text{ZrO}_4$  being a Ruddleson perovskite is a two-dimensional layered material and formation of three layers within this composite are visualized from front and side view as shown in Figure 2. These layers are labeled as L1, L2, and L3, where L1 and L3 are considered surface layers with L2 being middle layer or more specifically bulk layer. For a better understanding, the front and side view of this structure and its interface with TiN and TaN treated here as two different electrodes (along c axis) is displayed in Figure 1. Noting the basic structure of  $\text{Sr}_2\text{ZrO}_4$  in Figure 1, half of the total Sr atoms are present in layer 2 (L2) and forming a nine-fold geometry coordination shown by green highlighted region (polyhedral) in such a way that single  $\text{Sr}^{2+}$  atom is bonded to nine  $\text{O}^{2-}$  atoms. These  $\text{Sr}^{2+}$  atoms forming an intruding layer are present at the boundary between the perovskite layer and the intermediate blocking layer. Whereas the remaining half of the  $\text{Sr}^{2+}$  atoms present in layer 1 (L1) and layer 3 (L3) are a part of perovskite structural layer having Zr atom (of L2) as a B site cation. These  $\text{Sr}^{2+}$  atoms are forming twelve folded coordinations with twelve  $\text{O}^{2-}$  atoms. Comprehensive insight of the structural properties are displayed in Figure 1 confirmed that, in vertical stacking, only one perovskite layer shown by pink highlighted non-tilted  $\text{ZrO}_6$  octahedral is justified by the number of layers equivalent to “n” used in formula of Ruddleson perovskite  $\text{Sr}_{n+1}\text{Zr}_n\text{O}_{3n+1}$  (here  $n = 1$ ). Whereas,  $\text{Zr}^{4+}$  atoms in L1 and L3 are serving the separate perovskite structure and are part of the reported blocking layer of RP perovskite layered structure. Structure of the considered Ruddleson–Popper perovskite is in accordance with [25,34]. The bond length between Sr-O and Zr-O are not stacked to the same values in these layers as in Table 2. To instigate the interfacial effects more effectively,  $V_{\text{O}}$ s are introduced in this study in L1 in such a way that bond length between Sr-O and Zr-O is at its minimum as displayed in Table 2 and Figure 1 (with arrows). From the findings displayed in Table 2, it is clear that  $\text{Sr}_2\text{ZrO}_4/\text{TaN}$  showing lesser deviations in bond length and hence are expected to display comparatively better stability results.

Formation energy is considered an important parameter in deciding the RRAM properties such as stability, forming voltage, endurance, and retention. In this work, formation energy is calculated by introducing single and double  $V_{\text{O}}$ s in the nearest neighbor layer (L1) of electrode layer to maximize the interfacial effects. Negative values of formation energy (Figure 3) in absence and presence of  $V_{\text{O}}$ s confirm that considered composites are stable and can be prepared experimentally [54,55]. Change in formation energy of  $\text{Sr}_2\text{ZrO}_4$  after connecting with the electrode is attributed to the interfacial effects. It is also clear from Figure 3 that changes in formation energy of  $\text{Sr}_2\text{ZrO}_4/\text{TiN}$  after introducing the  $V_{\text{O}}$ s are not gradual but abrupt and may cause stability issues in attaining required stable RS state. On the other side, small and gradual changes in formation energy of  $\text{Sr}_2\text{ZrO}_4/\text{TaN}$  before and after introducing  $V_{\text{O}}$ s will assist in attaining the stable RS state and hence in overcoming the uniformity and variability issues caused by random changes. Moreover, it is also expected that smaller formation energy for  $\text{Sr}_2\text{ZrO}_4/\text{TaN}$  will make this system more stable, resulting in slowed down depletion of  $V_{\text{O}}$ s from the conducting filament. This may also result in slower  $V_{\text{O}}$ s diffusion rate. These results may assist in attaining stable LRS of RRAM and hence improve the retention properties by making the  $\text{LRS} \leftrightarrow \text{HRS}$  process robust. However, required forming voltage will become higher due to smaller formation energy and stability of the  $\text{Sr}_2\text{ZrO}_4/\text{TaN}$ .  $\text{Sr}_2\text{ZrO}_4/\text{TiN}$ -based RRAM devices will work with lower forming voltage due to higher formation energy; however with higher formation energy, this system may be unstable and may cause instability issues. Zhong et al. [14] reported the easy escape of oxygen from  $\text{HfO}_2$  system with TiN electrode in the atmosphere to form  $\text{O}_2$  molecule. They also reported the use of Ta layer above  $\text{HfO}_2$  to prohibit this escape and elucidated the movement of O atoms from  $\text{HfO}_2$  layer towards the interface of Ta/ $\text{HfO}_2$  and stayed

exhibiting stable RS. Fukuchi et al. [56] also reported the formation of rough granular paths formed by Ti metal at interface making the diffusion of anion harder. The whole of this discussion is confirming that nature of electrode influences the formation energy and hence retention properties and forming voltage of  $\text{Sr}_2\text{ZrO}_4$  being treated as RP layered perovskite-based RRAM devices.

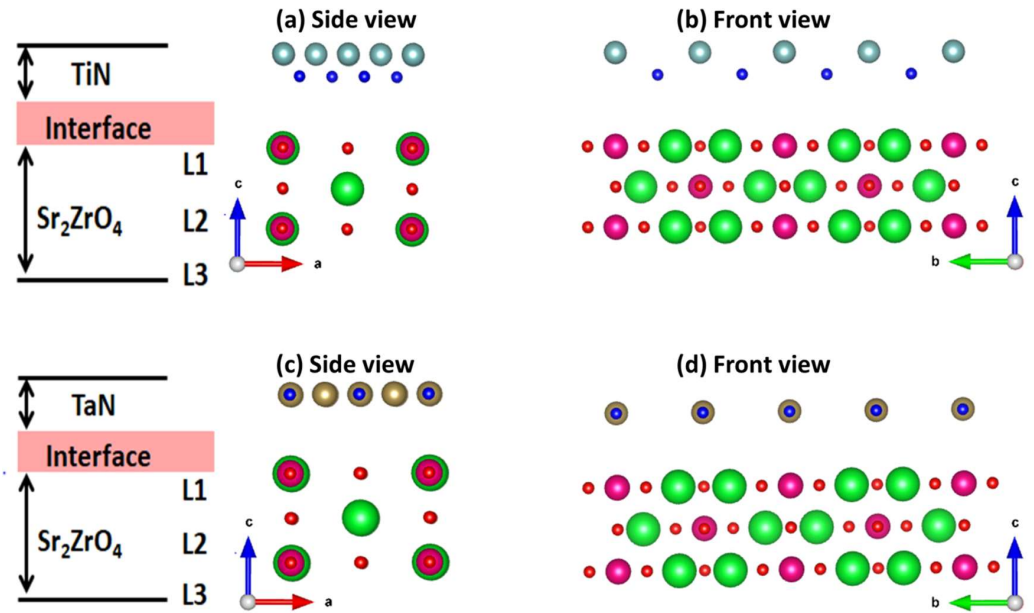


**Figure 2.** Side view and front view of (a,b)  $\text{Sr}_2\text{ZrO}_4/\text{TiN}$  and (c,d)  $\text{Sr}_2\text{ZrO}_4/\text{TaN}$  assuming the layers stacked along c axis. Three layers of the considered Ruddleson–Popper perovskite material ( $\text{Sr}_2\text{ZrO}_4$ ) and interface are labeled as L1, L2, L3 and interface, respectively. Color scheme of the atoms is same as described earlier in Figure 1.

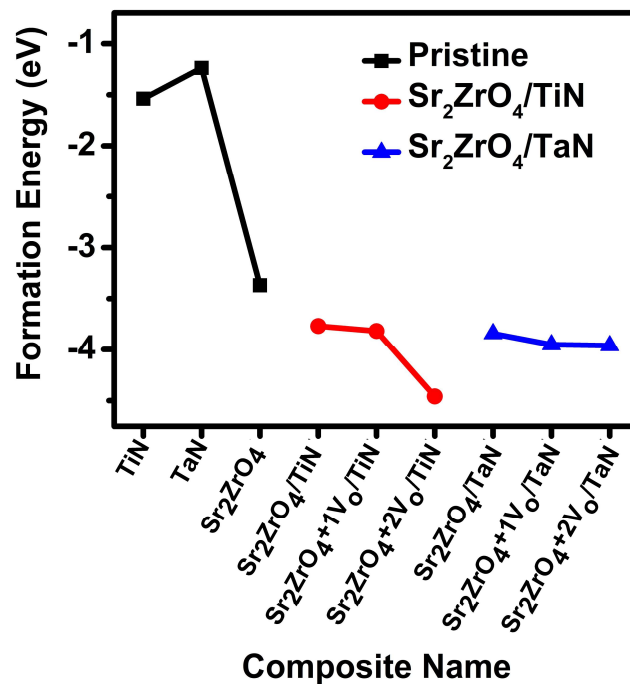


**Figure 3.** Formation energy of considered composites before and after making interfacial contacts.

### 3.2. Work Function

For better description of influence of TiN and TaN electrodes on conduction mechanism within the attached  $\text{Sr}_2\text{ZrO}_4$ RS-layered material and at the interface, potential lineups of electrodes (TiN and TaN),  $\text{Sr}_2\text{ZrO}_4$ , and  $\text{Sr}_2\text{ZrO}_4$ /electrode are displayed in Figure 4. Three layers of  $\text{Sr}_2\text{ZrO}_4$  at different energy values in work function (WF) plots displayed in Figure 4 are indicative of bottom of valence band (VB) of these specified three layers are at different potential energy (PE). Electrons present in the surface layers (L1 and L3) can easily participate in conduction mechanism owing to their lesser value of PE. Whereas electrons in the middle layer more typically bulk layer (L2) are strongly bounded with higher PE and contribute lesser in conduction mechanisms. This makes the rate of diffusion of trapped charged particles slower and result in stable LRS state for the improvement of retention properties of RRAM devices. In addition to it, two surface layers indicating the PE of valence band maximum have different PE, labeled as E1 and E2 in Figure 4. This creates an electric field ( $\Delta E = E_2 - E_1$ ) difference inside layered material where field value is higher at L1 and lower at L3. This field difference is owned by interfacial effects resulted from WF difference existing between RS layer and electrode material. This interfacial effect aligned the energy bands of RS layer and electrodes to attain equilibrium at interface and resulted in field difference between layers. Interfacial effects caused by WF difference also shifted the FL of electrode and RS layer to attain equilibrium at interface. Equilibrium position of the Fermi level of considered system can be seen below the FL of  $\text{Sr}_2\text{ZrO}_4$  and above the TiN (TaN) electrode in Figure 4. Comparatively higher shifting of FL at interface to attain equilibrium in case of  $\text{Sr}_2\text{ZrO}_4$ /TaN is indicating more reactive nature of TaN. It is also verdict from potential energy lineups that valence band bottom of TiN (TaN) electrodes and RS layer are existing at different potential energy and instinct in charge species to move. It is also verdict from potential line ups that charge conduction will be easier from TiN electrode towards RS layer than vice versa due to shallower valence band bottom of TiN. Consequently, movement of oxygen/ $V_{\text{O}}$ s from RS layer towards electrodes will become harder and more external field demanding. Zhong et al. [14] also reported that oxygen atom find easier to escape from  $\text{HfO}_2$  into atmosphere to form  $\text{O}_2$  molecule rather than to form filament at TiN/ $\text{HfO}_2$  interface. However, TaN electrode will gather oxygen at interface where, oxygen atoms will find it easier path to escape from RS layer due to shallower valence band bottom of RS layer.

### 3.3. Electronic Properties

Electronic properties of the considered systems are analyzed in detail using DOS, PDOS isosurface, and integrated charge density plots by employing DFT calculations to understand the physical picture of the conduction mechanism. Bader charge analysis and potential lineups are also calculated to understand charge redistribution phenomena. For this purpose, first of all, potential lineups are elaborated with potential lineups in the middle panel with their respective isosurface charge density plots in left and right panels in Figure 5. Yellow and cyan color in isosurface charge density plots are indicating charge accumulation and depletion, respectively. Isosurface charge density plots of pristine systems as shown in Figure 5a,c indicate the presence of quantized charge in three layers of  $\text{Sr}_2\text{ZrO}_4$  and TiN (TaN) electrode. Charge accumulation around "O" (red color ball) and "N" (blue color ball) indicates that N-O ionic bond and hence TiON (TaON) being a space charge limited (SCL) layer is formed at interface. It is expected that this SCL layer may stop the further movement of free charge carriers and hence switch the device to HRS and a forming free voltage is expected to be needed to change RS state of the two considered devices. Moreover, quantized conduction in all three layers of RP perovskite used as RS 2D-layered material will further widen this depletion layer and consequently dispersed charge trapping centers in the three layers may cause the uniformity issue. These findings are also verdict from potential lineups (Figure 5b), where three peaks labeled L1, L2, and L3 are indicating potential energies of valence electrons in three different layers of considered RP perovskite. With more potential energy, electrons are comparatively more strongly

quantized in L2 of RP perovskite layered structure and will resist strongly in changing the RS state of the device. It is also clear from this figure that valence band of TiN are shallower than TaN ( $\Delta E = 6.612$  eV) and provides the charges to move towards RS layer. However, with deeper valence band, TaN escapes O atoms from RS layer and hence contribute more towards interfacial effect enhancement by making the process of charge transfer from electrode towards RS layer easier. By creating a single  $V_o$  at interface in L1, potential energy of valence electrons in L1 becomes smaller than L2 and L3, accumulates more charge at interface by making the charge extracting mechanism easier and hence enhance low power consuming aspect of the considered systems. It is also clear that shifting up(down) of potential energy line of TiN (TaN) as shown in Figure 5e decreases(increases) the charge transfer from electrode towards considered RP perovskite. It is also worth mentioning here that nature of bonding in the RS layer also changed from ionic to covalent between Sr and O atoms with charge redistribution appearance at interstitial sites. Previous studies reported the presence of electropositive and electronegative layers formed by "A" and "B" site cation in  $A_2BO_4$  RP perovskite with a tendency to accommodate excess oxide ions and holes owing to their electropositive and electronegative nature, respectively. It is also reported that this excess charge will tend to accumulate at interstitial site to facilitate the neutrality of electronic polarity of layers [42,57,58]. These findings support the charge accumulated in the interstitial sites around "Sr" atom at interface and hence stability of RS state in considered RRAM devices. Moreover, it is expected that "Zr" is showing its tendency to change its valence state as Xavier et al. [59] reported Valence change in cationic lattice due to  $V_o$ s. Noted the diameter of conducting filament of  $V_o$ s falling into atomic scale, conduction may be expected to quantize in considered 2D layered material as elaborated in ref. [18]. In isosurface charge density plots (Figure 5d,f); interfacial effects are present in case of TiN electrode with more charge redistribution at interface and are attributed to smaller potential energy lineups of TiN and L1. However conductivity of L2 and L3 decreased but persists and hence TiN electrode may assist in attaining the gradual switching resistance of  $Sr_2ZrO_4/TiN$ . The presence of a charge redistribution in L2 and L3 may also cause leakage and a current problem and hence cross talk problems in cross point arrays of RRAM devices. Whereas, TaN reduced the conductivity of L2 and L3 more effectively, quantized it on L1/TaN interface and hence may assist to overcome the cross talk related issues. These results are enhanced further with increasing concentration of  $V_o$ s (here  $2V_o$ s) as shown in Figure 5g–i. Note that TaN not only reduced the conductivity of vertically stacked L2 and L3 bulk layers but also lateral conductivity of L1 away from  $V_o$ s. Highly confined conductivity near the  $V_o$ s will assist in attaining the highly confined  $V_o$ s based conducting filament and hence LRS. Reduced conductivity of the L2 and L3 will decrease the width of depletion layer and hence may increase the ability to store charges in accordance to the inverse relation between ability to store charges and depletion width layer [8]. These theoretical findings confirm the optimized switching owned by modified interfacial effects may also assist in overcoming the uniformity and variability issues of RRAM devices. Fukuchi et al. [56] also reported the formation of better enriched oxygen reservoir at interface by Ta as compared to Ti metal facilitating the diffusion of anions in their studied 2D RS material.

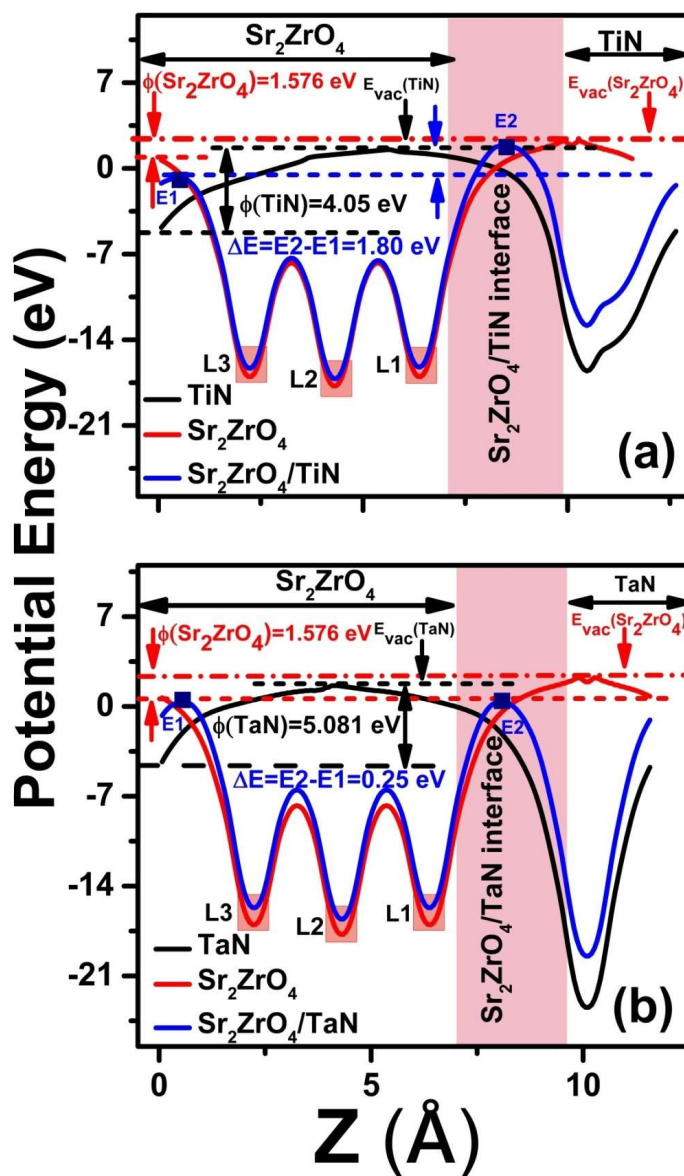


**Figure 4.** Potential energy lineups of pristine (a)  $\text{Sr}_2\text{ZrO}_4$ , TiN,  $\text{Sr}_2\text{ZrO}_4/\text{TiN}$  and (b)  $\text{Sr}_2\text{ZrO}_4$ , TaN and  $\text{Sr}_2\text{ZrO}_4/\text{TaN}$ . Pink highlighted region labelled L1, L2 and L3 as an indicative of three layers formed inside the  $\text{Sr}_2\text{ZrO}_4$  layered Ruddleson–Popper perovskite structures.

Integrated charge density plots of the considered composites along with respective Bader charge analysis are displayed in Figure 6. Positive values and negative values of integrated charge density explains the variations of positive and negative electron density along z-axis as displayed in Figure 6. Three distinct peaks as shown by highlighted regions in Figure 6b with positive values are indicative of charge accumulated and hence quantized conduction in the three layers (L1, L2, and L3) of  $\text{Sr}_2\text{ZrO}_4$ . Whereas, at interface of RS material and electrode (6.8 Å–10 Å), charge redistribution is observed near electrode (as shown by highlighted region in Figure 6b). The dominating integrated charge redistribution peak is indicating the better oxygen scavenging capability of TaN electrode as ascribed in potential energy lineups and isosurface charge density plots. The respective Bader charge analysis as shown in Figure 6a,c also confirmed charge accumulated by “O” and “N” atoms with negative Bader charge value and depleted by Sr, Zr, Ti, and Ta atoms. The negative (positive) Bader charge value is verdict of anionic (cationic) nature of “N” and “O” (Zr, Sr, Ti, and Ta) atoms. This can be seen in the form of charge accumulated around “N”

atoms of both electrodes and “O” atoms of RS material present near the interface forming interfacial TiON(TaON) layer in isosurface charge density plots (Figure 5a,c). By creating single  $V_o$  in  $Sr_2ZrO_4$  layer near the interface as shown in Figure 6e, the conductivity of the L2 and L3 reduced and charge became localized near the  $V_o$  in the vicinity of RS layer-electrode interface in L1 with single dominating positive peak. The reduced peak value of integrated charge density plot confirmed the reduced conductivity of the whole system. With  $2V_o$ s, interfacial conductivity increased again and interfacial layer L1 localized the maximum charge after extracting from L2, L3, and TiN (TaN) electrode as elucidated with only positive peak as shown in Figure 6h. It is also clear that among the two considered systems, TaN localized more charge by reducing the conductivity of bulk layers L2 and L3 and participated more actively in achieving the desired quantizing conduction. Evidently, TaN is more effective in increasing the interfacial conductivity and hence reducing the contact resistance. It is also clear from IC plot in Figure 6e,h that CFs formed by  $V_o$ s in isosurface charge density plots (Figure 5) are of the order of few angstroms i.e., nano-scale to atomic unit and hence quantized conduction. On the basis of results reported on quantized conduction in refs. [19,20], area of considered devices can be scaled down up to nanometers to achieve remarkable RS performance by overcoming reliability and variability issues. Bader charge analysis in the respective figures again showed the above demonstrated behavior with slight changes involved in just Bader charge values attained by each atom.

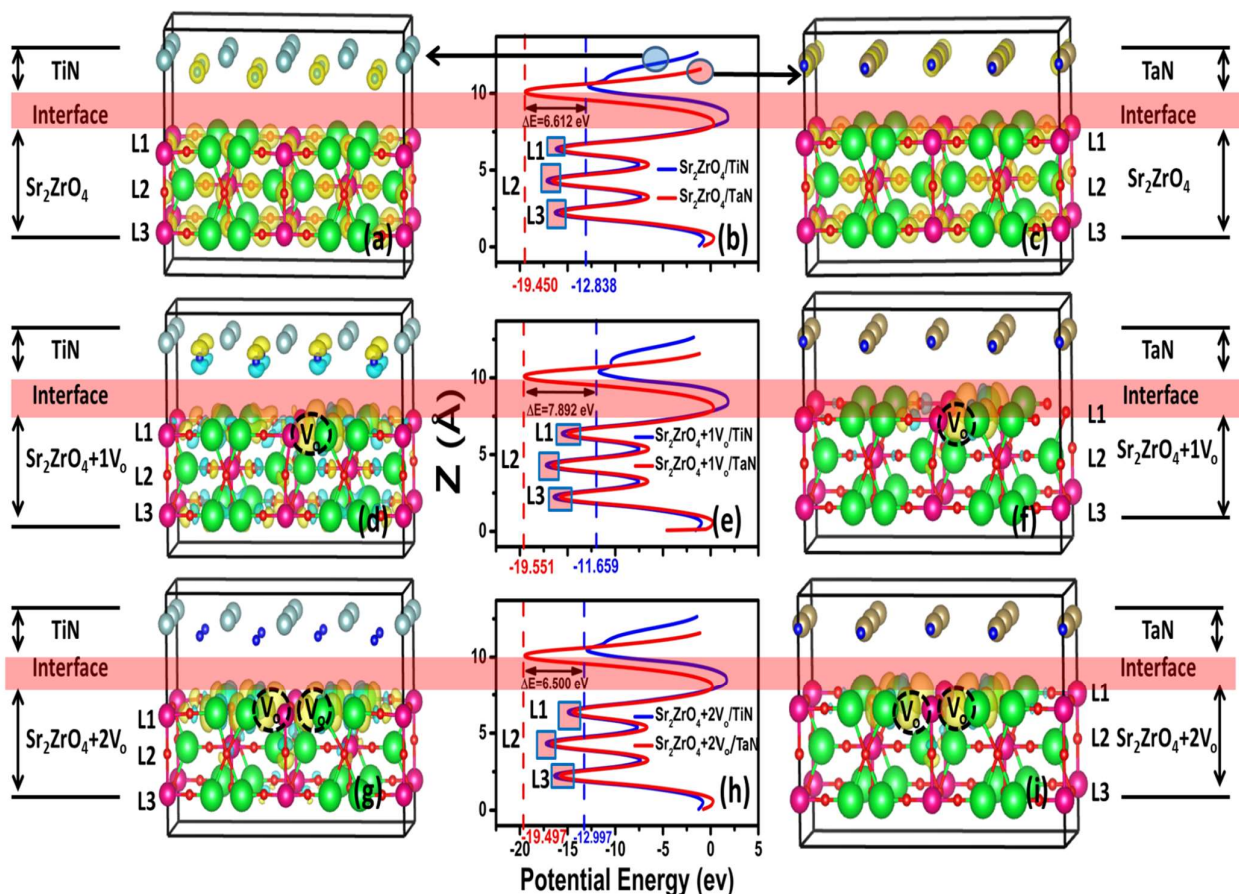


**Figure 5.** Potential energy lineups in middle panel and their respective isosurface charge density plot in left and right panel for (a–c) pristine (d–f) pristine +  $1V_o$  (g–i) pristine +  $2V_o$  2D layered RP perovskite structures.

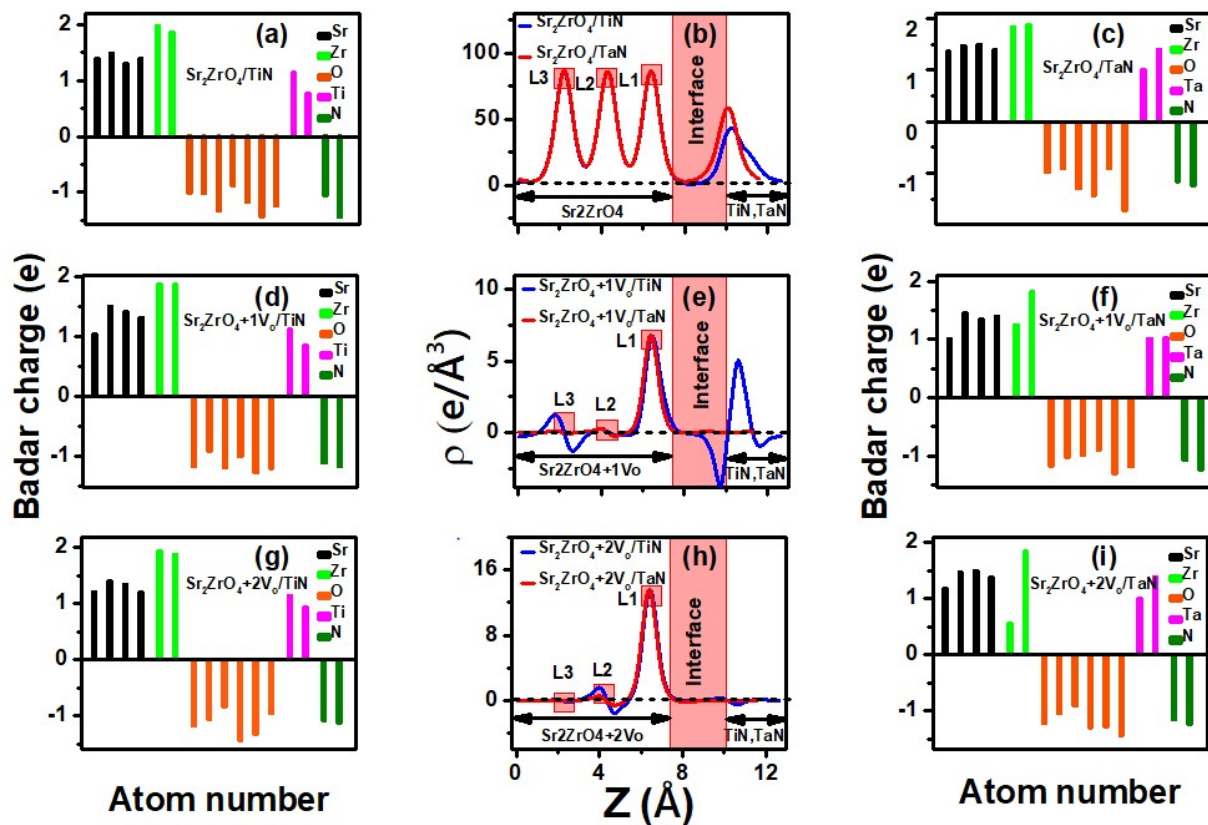


**Figure 6.** Integrated charge density plots in middle panel and their respective Bader charge analysis in left and right panel for (a–c) pristine (d–f) pristine +  $1V_o$  (g–i) pristine +  $2V_o$  2D layered RP perovskite structures.

Detailed insight of electronic properties in terms of DOS (middle panel) and their respective PDOS (specified by highlighted circle and arrow in left and right panel) spectra is presented in Figure 7. In these plots, FL is indicated by a black dashed line and left and right region of FL are VB and conduction band (CB), respectively. It is indicated from Figure 7b that both pristine systems are conductive in nature with nonzero localized defect states present near and around the FL. Reasoning of each localized state in VB and CB of DOS is the verdict from elemental behavior of individual atom in PDOS. It is justified from PDOS spectra that “O” atom of RP layered RS composite and N and Ti(Ta) atom of TiN (TaN) electrode are playing comparatively more dominating role. This resulting in strong overlapping of orbitals and hence resulted in TiON (TaON) layer observed in isosurface charge density plots (Figure 5). Whereas localized states in PDOS of Zr atom are pointing towards its tendency to change its valence state as a result of oxidation occurring at interface. Work function, ICD plots, and Bader charge analysis also confirmed this conducting behavior of composites at interface. On creating the single  $V_o$  in RP-layered RS composite, conductivity of the considered composite decreased in both cases with lesser localized states in VB as well as CB of respective DOS plot (Figure 7e). Whereas conductivity increased again by increasing concentration of  $V_o$ s ( $2V_o$ s here) with again increased localized state in DOS plots (Figure 7h). It is also indicated from the PDOS of the two later cases that presence of  $V_o$ s effected the local conductivity of considered systems and localized states of Zr (nearest neighbor of  $V_o$ s) and Ti(Ta)atom became more dominating than any other constituent of the considered composites in Figure 7 within the energy  $-0.5$ – $0.5$  eV around the FL. This also confirmed the important role of  $V_o$ s based conductance quantization in localizing the states of Zr and Ti(Ta) atoms near the FL in VB and CB, respectively. This also confirmed the fact that the  $Zr^{4+}$  atom tended to change

its valence state to  $Zr^{2+}$  to maintain the neutrality and hence stability of the system in the presence of  $V_{Os}$ . These results confirmed the stability of LRS and HRS attained in system.

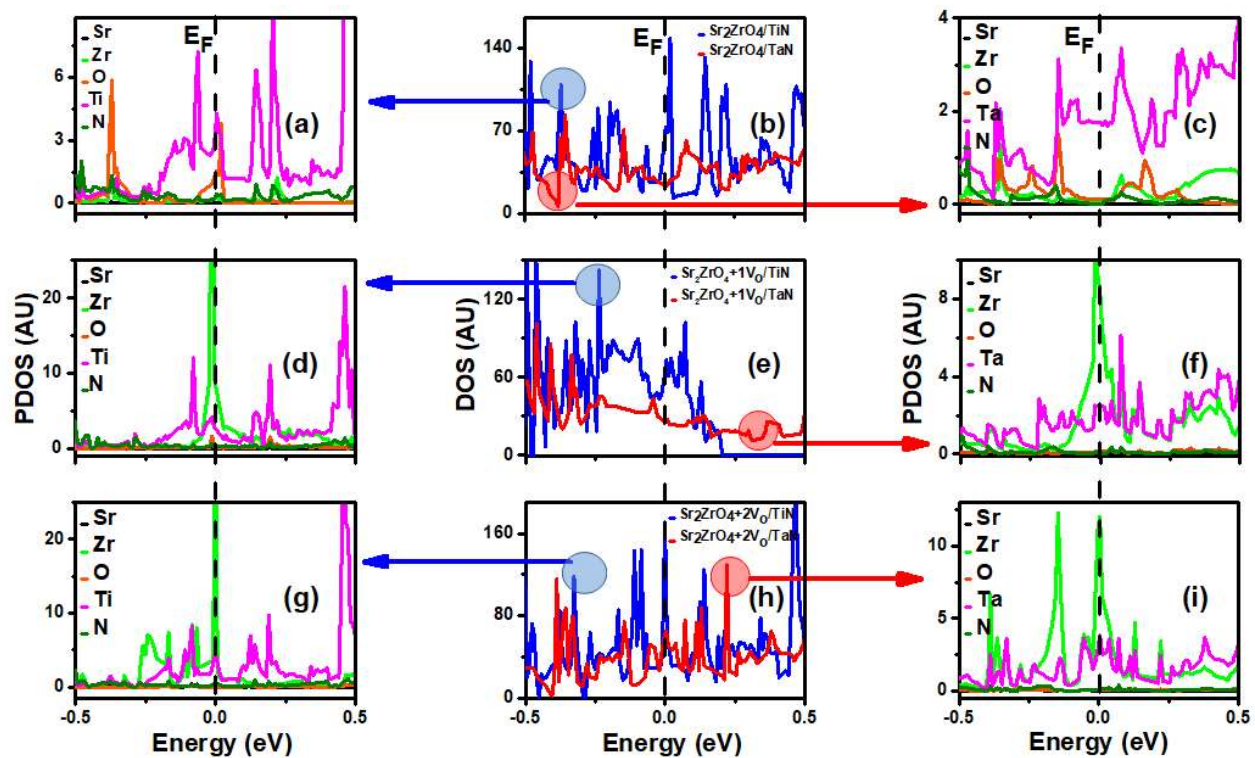


**Figure 7.** DOS in middle panel and their respective PDOS in left and right panel for (a–c) pristine (d–f) pristine +  $1V_o$  (g–i) pristine +  $2V_o$  2D layered RP perovskite structures.

#### 4. Conclusions

In this first principles study, the concept of quantized conduction is explored for interfacial RS application by analyzing the size of  $V_{Os}$ -based conducting filaments. To make the findings closer to experimental results,  $Sr_2ZrO_4/TiN$  and  $Sr_2ZrO_4/TaN$  heterostructures were modeled while treating the TiN and TaN as an electrode. The size of the conducting filaments within the range of atomic units in integrated charge density plots confirmed the occurrence of quantized conduction in  $Sr_2ZrO_4$  being a Ruddleson–Popper 2D-layered material. The isosurface charge density and density of states also confirmed the presence of localized charge and hence quantized conduction in  $Sr_2ZrO_4$  owned by  $V_{Os}$ . Bader charge analysis and PDOS confirmed the redistribution owned by constituent atoms. Detailed insight of  $Sr_2ZrO_4/TiN$  and  $Sr_2ZrO_4/TaN$  heterostructure interface is provided by calculating the charge redistribution from potential lineups. The interface of these two layered heterostructures revealed the modified electronic properties which cannot be achieved with either layer alone. Findings of these calculations confirmed that TaN is more effective in attaining quantized conduction and forming TaON layer at heterostructure interface. Formation energy results confirmed that resistive switching state attained by TaN electrode is more stable than TiN. These results predict the improved retention and stability performance of RRAM devices.

**Author Contributions:** Conceptualization, M.I. and F.H.; Methodology, M.I., F.H. and R.M.A.K.; Validation, A.S.; Formal analysis, U.R., N.A.N., R.M.A.K. and M.A.; Investigation, M.I. and S.M.E.; Resources, S.M.E.; Data curation, U.R., F.H. and M.A.; Writing—original draft, U.R.; Writing—review & editing, M.I.; Visualization, U.R. and A.S.; Supervision, F.H. All authors have read and agreed to the published version of the manuscript.

**Funding:** This research was funded by Sayed M Eldin, Center of Research, Faculty of Engineering and Technology, Future University in Egypt New Cairo 11835 Egypt.

**Data Availability Statement:** The data presented in this study are available on reasonable request from the corresponding author.

**Conflicts of Interest:** The authors declare no conflict of interest.

## References

1. Han, J.S.; Le, Q.V.; Choi, J.; Kim, H.; Kim, S.G.; Hong, K.; Moon, C.W.; Kim, T.L.; Kim, S.Y.; Jang, H.W. Lead-free all-inorganic cesium tin iodide perovskite for filamentary and interface-type resistive switching toward environment-friendly and temperature-tolerant nonvolatile memories. *ACS Appl. Mater. Interfaces* **2019**, *11*, 8155–8163. [[CrossRef](#)] [[PubMed](#)]
2. Shi, Y.; Liang, X.; Yuan, B.; Chen, V.; Li, H.; Hui, F.; Yu, Z.; Yuan, F.; Pop, E.; Wong, H.S.P.; et al. Electronic synapse made of layered two-dimensional materials. *Nat. Electron.* **2018**, *1*, 458–465. [[CrossRef](#)]
3. Zhou, Z.; Yang, F.; Wang, S.; Wang, L.; Wang, X.; Wang, C.; Xie, Y.; Liu, Q. Emerging of two dimensional materials in novel memristor. *Front. Phys.* **2022**, *17*, 23204. [[CrossRef](#)]
4. Duan, H.; Cheng, S.; Qin, L.; Zhang, X.; Xie, B.; Zhang, Y.; Jie, W. Low-Power Memristor Based on Two-Dimensional Materials. *J. Phys. Chem. Lett.* **2022**, *13*, 7130–7138. [[CrossRef](#)]
5. Jagath, A.L.; Leong, C.H.; Kumar, T.N.; Almurib, H.A.F. Insight into physics-based RRAM models—Review. *J. Eng.* **2019**, *2019*, 4644–4652. [[CrossRef](#)]
6. Kai, D.S.; Fang, H.X.; Dan, W.L.; Dong, L.C.; Pinaki, M. Memristor-based RRAM with applications. *Sci. China Inf. Sci.* **2012**, *55*, 1447–1460.
7. Sun, L.; Hao, X.; Meng, Q.; Wang, L.; Liu, F.; Zhou, M. Polaronic resistive switching in ceria-based memory devices. *Adv. Electron. Mater.* **2019**, *5*, 1900271. [[CrossRef](#)]
8. Sawa, A. Resistive switching in transition metal oxides. *Mater. Today* **2008**, *11*, 28–36. [[CrossRef](#)]
9. Tsui, S.; Baikalov, A.; Cmaidalka, J.; Sun, Y.Y.; Wang, Y.Q.; Xue, Y.Y. Field-induced resistive switching in metal-oxide interfaces. *Appl. Phys. Lett.* **2004**, *85*, 317. [[CrossRef](#)]
10. Seong, D.J.; Jo, M.; Lee, D.; Hwang, H. HPHA effect on reversible resistive switching of Pt/Nb-doped SrTiO<sub>3</sub>Schottky junction for nonvolatile memory application electrochem. *Solid State Lett.* **2007**, *10*, H168. [[CrossRef](#)]
11. Nian, Y.B.; Strozier, J.; Wu, N.J.; Chen, X.; Ignatiev, A. Evidence for an Oxygen Diffusion Model for the Electric Pulse Induced Resistance Change Effect in Transition-Metal Oxides. *Phys. Rev. Lett.* **2007**, *98*, 146403. [[CrossRef](#)] [[PubMed](#)]
12. Ismail, M.; Khan, S.A.; Rahmani, M.K.; Choi, J.; Batool, Z.; Rana, A.M.; Kim, S. Oxygen annealing effect on resistive switching characteristics of multilayer CeO<sub>2</sub>/Al/CeO<sub>2</sub> resistive random-access memory. *Mater. Res. Express* **2020**, *7*, 016307. [[CrossRef](#)]
13. Asif, M.; Kumar, A. Resistive switching in emerging materials and their characteristics for neuromorphic computing. *Mater. Today Electron.* **2022**, *1*, 100004. [[CrossRef](#)]
14. Zhong, X.; Rungger, I.; Zapol, P.; Nakamura, H.; Asai, Y.; Heinonen, O. The effect of a Ta oxygen scavenger layer on HfO<sub>2</sub>-based resistive switching behavior: Thermodynamic stability, electronic structure, and low-bias transport. *Phys. Chem. Chem. Phys.* **2016**, *18*, 7502–7510. [[CrossRef](#)] [[PubMed](#)]
15. Rasheed, U.; Ryu, H.; Mahata, C.; Khalil, R.M.A.; Imran, M.; Rana, A.M.; Kousar, F.; Kim, B.; Kim, Y.; Cho, S.; et al. Resistive switching characteristics and theoretical simulation of a Pt/aTa<sub>2</sub>O<sub>5</sub>/TiN synaptic device for neuromorphic applications. *J. Alloys Compd.* **2021**, *877*, 160204. [[CrossRef](#)]
16. Mikhaylov, A.; Belov, A.; Korolev, D.; Antonov, I.; Kotomina, V.; Kotina, A.; Gryaznov, E.; Sharapov, A.; Koryazhkina, M.; Kryukov, R.; et al. Multilayer metal-oxide memristive device with stabilized resistive switching. *Adv. Mater. Technol.* **2020**, *5*, 1900607. [[CrossRef](#)]
17. Yang, H.C.; Seidel, J.; Kim, S.Y.; Rossen, P.B.; Yu, P.; Gajek, M.; Chu, Y.H.; Martin, L.W.; Holcomb, M.B.; He, Q.; et al. Electric modulation of conduction in multiferroic Ca-doped BiFeO<sub>3</sub> films. *Nat. Mater.* **2009**, *8*, 485–493. [[CrossRef](#)]
18. Gao, S.; Zeng, F.; Chen, C.; Tang, G.; Lin, Y.; Zheng, Z.; Song, C.; Pan, F. Conductance quantization in a Ag filament-based polymer resistive memory. *Nanotechnology* **2013**, *24*, 335201. [[CrossRef](#)]
19. Li, Y.; Long, S.; Liu, Y.; Hu, C.; Teng, J.; Liu, Q.; Lv, H.; Sune, J.; Liu, M. Conductance Quantization in Resistive Random Access Memory. *Nanoscale Res. Lett.* **2015**, *10*, 420. [[CrossRef](#)]
20. Krishnan, K.; Muruganathan, M.; Tsuruoka, T.; Mizuta, H.; Aono, M. Highly reproducible and regulated conductance quantization in a polymer-based atomic switch. *Adv. Funct. Mater.* **2017**, *27*, 1605104. [[CrossRef](#)]
21. Rehman, M.M.; Rehman, H.M.M.U.; Gul, J.Z.; Kim, W.Y.; Karimov, K.S.; Ahmed, N. Decade of 2D-materials-based RRAM devices: A review. *Sci. Technol. Adv. Mater.* **2020**, *21*, 147–186. [[CrossRef](#)] [[PubMed](#)]

22. Liao, K.; Lei, P.; Tu, M.; Luo, S.; Jiang, T.; Jie, W.; Hao, J. Memristor based on inorganic and organic two-dimensional materials: Mechanisms, performance, and synaptic applications. *ACS Appl. Mater. Interfaces* **2021**, *13*, 32606–32623. [[CrossRef](#)] [[PubMed](#)]
23. Sun, K.; Chen, J.; Yan, X. The future of memristors: Materials engineering and neural networks. *Adv. Funct. Mater.* **2021**, *31*, 2006773. [[CrossRef](#)]
24. Wang, M.; Cai, S.; Pan, C.; Wang, C.; Lian, X.; Zhuo, Y.; Xu, K.; Cao, T.; Pan, X.; Wang, B.; et al. Robust memristors based on layered two-dimensional materials. *Nat. Electron.* **2018**, *1*, 130–136. [[CrossRef](#)]
25. Li, Y.; Loh, L.; Li, S.; Chen, L.; Li, B.; Bosman, M.; Ang, K.W. Anomalous resistive switching in memristors based on two dimensional palladium diselenide using heterophase grain boundaries. *Nat. Electron.* **2021**, *4*, 348–356. [[CrossRef](#)]
26. Chen, S.; Mahmoodi, M.R.; Shi, Y.; Mahata, C.; Yuan, B.; Liang, X.; Wen, C.; Hui, F.; Akinwande, D.; Strukov, D.B.; et al. Wafer scale integration of two-dimensional materials in high-density memristive crossbar arrays for artificial neural networks. *Nat. Electron.* **2020**, *3*, 638–645. [[CrossRef](#)]
27. Feng, X.; Li, Y.; Wang, L.; Chen, S.; Yu, Z.G.; Tan, W.C.; Macadam, N.; Hu, G.; Huang, L.; Chen, L.; et al. A fully printed flexible MoS<sub>2</sub> memristive artificial synapse with femto joule switching energy. *Adv. Electron. Mater.* **2019**, *5*, 1900740. [[CrossRef](#)]
28. Lu, X.F.; Zhang, Y.; Wang, N.; Luo, S.; Peng, K.; Wang, L.; Chen, H.; Gao, W.; Chen, X.H.; Bao, Y.; et al. Exploring low power and ultrafast memristor on p-type van der waalsSnS. *Nano Lett.* **2021**, *21*, 8800–8807. [[CrossRef](#)]
29. Cao, G.; Meng, P.; Chen, J.; Liu, H.; Bian, R.; Zhu, C.; Liu, F.; Liu, Z. 2D Material Based Synaptic Devices for Neuromorphic Computing. *Adv. Funct. Mater.* **2021**, *31*, 2005443. [[CrossRef](#)]
30. Lee, T.S.; Lee, N.J.; Abbas, H.; Hu, Q.; Yoon, T.S.; Lee, H.H.; Shim, E.L.; Kang, C.J. A study on the resistance switching of Ag<sub>2</sub>Se and Ta<sub>2</sub>O<sub>5</sub> heterojunctions using structural engineering. *Nanotechnology* **2018**, *29*, 035202. [[CrossRef](#)]
31. Yuan, B.; Liang, X.; Zhong, L.; Shi, Y.; Palumbo, F.; Chen, S.; Hui, F.; Jing, X.; Villena, M.A.; Jiang, L.; et al. 150 nm × 200 nm cross-point hexagonal boron nitride-based memristors. *Adv. Electron. Mater.* **2020**, *6*, 1900115. [[CrossRef](#)]
32. Li, X.D.; Chen, N.K.; Wang, B.Q.; Li, X.B. Conductive mechanism in memristor at the thinnest limit: The case based on monolayer boron nitride. *Appl. Phys. Lett.* **2022**, *121*, 073505. [[CrossRef](#)]
33. Yan, X.; Zhao, Q.; Chen, A.P.; Zhao, J.; Zhou, Z.; Wang, J.; Wang, H.; Zhang, L.; Li, X.; Xiao, Z.; et al. Vacancy-induced synaptic behavior in 2D WS<sub>2</sub> nanosheet-based memristor for low-power neuromorphic computing. *Small* **2019**, *15*, 1901423. [[CrossRef](#)] [[PubMed](#)]
34. Li, S.; Pam, M.E.; Li, Y.; Chen, L.; Chien, Y.C.; Fong, X.; Chi, D.; Ang, K.W. Wafer-scale 2D hafnium diselenide based memristors crossbar array for energy-efficient neural network hardware. *Adv. Mater.* **2022**, *34*, 2103376. [[CrossRef](#)]
35. Lei, P.; Duan, H.; Qin, L.; Wei, X.; Tao, R.; Wang, Z.; Guo, F.; Song, M.; Jie, W.; Hao, J. High-performance memristor based on 2D layered BiOI nanosheet for low-power artificial optoelectronic synapses. *Adv. Funct. Mater.* **2022**, *32*, 2201276. [[CrossRef](#)]
36. Tian, H.; Guo, Q.; Xie, Y.; Zhao, H.; Li, C.; Cha, J.J.; Xia, F.; Wang, H. Anisotropic black phosphorus synaptic device for neuromorphic applications. *Adv. Mater.* **2016**, *28*, 4991–4997. [[CrossRef](#)]
37. Xiang, D.; Cao, Y.; Wang, K.; Han, Z.; Liu, T.; Chen, W. Artificially created interfacial states enabled van der Waals heterostructure memory device. *Nanotechnology* **2022**, *33*, 175201. [[CrossRef](#)]
38. Xiang, H.; Liu, P.; Ran, R.; Wang, W.; Zhou, W.; Shao, Z. Two-dimensional Dion-Jacobson halide perovskites as new-generation light absorbers for perovskite solar cells. *Renew. Sustain. Energy Rev.* **2022**, *166*, 112614. [[CrossRef](#)]
39. Huang, P.; Kazim, S.; Wang, M.; Ahmad, S. Toward Phase Stability: Dion–Jacobson Layered Perovskite for Solar Cells. *ACS Energy Lett.* **2019**, *4*, 2960–2974. [[CrossRef](#)]
40. Luo, T.; Zhang, Y.; Xu, Z.; Niu, T.; Wen, J.; Lu, J.; Jin, S.; Liu, S.F.; Zhao, K. Compositional Control in 2D Perovskites with Alternating Cations in the Interlayer Space for Photovoltaics with Efficiency over 18%. *Adv. Mater.* **2019**, *31*, 1903848. [[CrossRef](#)]
41. Ahmad, S.; Fu, P.; Yu, S.; Yang, Q.; Liu, X.; Wang, X.; Wang, X.; Guo, X.; Li, C. Dion-Jacobson Phase 2D Layered Perovskites for Solar Cells with Ultrahigh Stability. *Joule* **2019**, *3*, 794–806. [[CrossRef](#)]
42. Nirala, G.; Yadav, D.; Upadhyay, S. Ruddlesden–Popper phase A<sub>2</sub>BO<sub>4</sub> oxides: Recent studies on structure, electrical, dielectric, and optical properties. *J. Adv. Ceram.* **2020**, *9*, 129–148. [[CrossRef](#)]
43. Beznosikov, B.V.; Aleksandrov, K.S. Perovskite-like crystals of the Ruddlesden–Popper series. *Crystallogr. Rep.* **2000**, *45*, 792–798. [[CrossRef](#)]
44. Sun, B.; Guo, T.; Zhou, G.; Wu, J.; Chen, Y.; Zhou, Y.N.; Wu, Y.A. A battery-like self selecting biomemristor from earth-abundant natural biomaterials. *ACS Appl. Biol. Mater.* **2021**, *4*, 1976–1985. [[CrossRef](#)] [[PubMed](#)]
45. Perdew, J.P.; Burke, K.; Ernzerhof, M. Generalized gradient approximation made simple. *Phys. Rev. Lett.* **1996**, *77*, 3865–3868. [[CrossRef](#)] [[PubMed](#)]
46. Blochl, P.E. Projector augmented-wave method. *Phys. Rev. B Condens. Matter.* **1994**, *50*, 17953–17979. [[CrossRef](#)]
47. Joubert, D. From ultrasoft pseudopotentials to the projector augmented-wave method. *Phys. Rev. B* **1999**, *59*, 1758–1775.
48. Hussain, F.; Imran, M.; Rana, A.M.; Khalil, R.M.A.; Khera, E.A.; Kiran, S.; Javid, M.A.; Sattar, M.A.; Ismail, M. An insight into the dopant selection for CeO<sub>2</sub>-based resistive-switching memory system: A DFT and experimental study. *Appl. Nanosci.* **2018**, *8*, 839–851. [[CrossRef](#)]
49. Darancet, P.; Millis, A.J.; Marianetti, C.A. Three-dimensional metallic and two-dimensional insulating behavior in octahedral tantalum dichalcogenides. *Phys. Rev. B* **2014**, *90*, 045134. [[CrossRef](#)]
50. Lan, G.; Song, J.; Yang, Z. A linear response approach to determine Hubbard U and its application to evaluate properties of Y<sub>2</sub>B<sub>2</sub>O<sub>7</sub>, B=transition metals 3d, 4d and 5d. *J. Alloys Compd.* **2018**, *749*, 909–925. [[CrossRef](#)]

51. Krukau, A.V.; Vydrov, O.A.; Izmaylov, A.F.; Scuseria, G.E. Influence of the exchange screening parameter on the performance of screened hybrid functionals. *J. Chem. Phys.* **2006**, *125*, 224106. [[CrossRef](#)] [[PubMed](#)]
52. Monkhorst, H.J.; Pack, J.D. Special points for Brillouin-zone integrations. *Phys. Rev. B.* **1976**, *13*, 5188–5192. [[CrossRef](#)]
53. Pack, J.D.; Monkhorst, H.J. Special points for Brillouin-zone integrations—A reply. *Phys. Rev. B.* **1977**, *16*, 1748–1749. [[CrossRef](#)]
54. Yang, F.; Yang, L.; Changzhi, A.; Xie, P.; Lin, S.; Wang, C.Z.; Lu, X. Tailoring bandgap of perovskite BaTiO<sub>3</sub> by transition metals co-doping for visible-light photoelectrical applications: A first-principles study. *Nanomaterials* **2018**, *8*, 455. [[CrossRef](#)] [[PubMed](#)]
55. Rasheed, U.; Alsuwian, T.; Imran, M.; Algadi, H.; Khera, E.A.; Khalil, R.M.A.; Mahata, C.; Hussain, F. Density functional theory insight into metal ions and vacancies for improved performance in storage devices. *Int. J. Energy Res.* **2021**, *45*, 1–13. [[CrossRef](#)]
56. Fukuchi, A.T.; Nakagawa, R.; Arita, M.; Takahashi, Y. Smooth interfacial scavenging for resistive switching oxide via the formation of highly uniform layers of amorphous TaOx. *ACS Appl. Mater. Interfaces* **2018**, *10*, 5609–5617. [[CrossRef](#)]
57. Zhao, H.; Li, Q.; Sun, L.P. Ln<sub>2</sub>MO<sub>4</sub> cathode materials for solid oxide fuel cells. *Sci. China Chem.* **2011**, *54*, 898–910. [[CrossRef](#)]
58. Choynet, J.; Mouron, P.; Crespin, M.; Aken, P.A.V.; Muller, W.F. Perovskite-like intergrowth structure of the reduced cuprate Nd<sub>2</sub>CuO<sub>3.5</sub>: A combination of defect and excess oxygen non-stoichiometry phenomena. *J. Mater. Chem.* **1994**, *4*, 895–898. [[CrossRef](#)]
59. Cartoixa, X.; Rurali, R.; Sune, J. Transport properties of oxygen vacancy filaments in metal/crystalline or amorphous HfO<sub>2</sub>/metal structures. *Phys. Rev. B* **2012**, *86*, 165445. [[CrossRef](#)]